Dalton Transactions

ROYAL SOCIETY OF CHEMISTRY

PAPER

View Article Online
View Journal | View Issue

Cite this: *Dalton Trans.*, 2026, **55**, 5283

Scalable metal–organic frameworks for efficient low concentration CO_2 capture under humid flue gas conditions

Thibaud Aumond, Mickaele Bonneau,* Corentin Collomb, Cécile Daniel and David Farrusseng

The global energy supply still largely relies on fossil fuels, whose combustion releases significant amounts of carbon dioxide (CO_2), the primary anthropogenic greenhouse gas linked to climate change. Adsorption on solid porous materials offers a promising alternative to conventional amine-based systems for CO_2 capture from industrial flue gases. While various materials, including zeolites and metal–organic frameworks (MOFs), have been extensively studied for high-concentration CO_2 streams, post-combustion capture at low concentrations (below 5% CO_2) under realistic conditions with water vapor remains poorly explored. Material selection requires balancing CO_2 adsorption capacity against water affinity, as strong hydrophilicity deteriorates regeneration efficiency. The challenge is to identify scalable, environmentally friendly materials that maintain high CO_2 selectivity under realistic flue gas conditions containing both low CO_2 concentrations and significant water vapor. Here, we show that CALF-20, a scalable MOF, exhibits superior CO_2 adsorption selectivity and regenerability compared to other tested materials, both in dry and humid conditions. Under dynamic breakthrough conditions using 2.5% CO_2 and 50% relative humidity, CALF-20 maintained a high CO_2 uptake (1.49 mmol g^{-1}) consistent with static isotherm data, and demonstrated complete regenerability at 80 °C without loss of performance over multiple cycles. These results directly contrast with hydrophilic zeolites, which, despite high raw CO_2 capacities, are unsuitable under realistic, humid flue gas. Our results under industrially relevant post-combustion conditions demonstrate that low water affinity combined with moderate CO_2 capacity outperforms high-capacity hydrophilic materials. This approach represents an effective pathway for CO_2 capture under realistic conditions and provides valuable insights for the development of selective, robust, and scalable CO_2 adsorbents. Such developments are expected to contribute significantly to reducing atmospheric CO_2 emissions and addressing climate change mitigation targets in the coming years.

Received 3rd February 2026,
Accepted 10th March 2026

DOI: 10.1039/d6dt00282j

rsc.li/dalton

Introduction

The global energy supply still largely relies on fossil fuels such as petroleum, coal, and natural gas, which remain the backbone of modern industrial and transportation energy systems. However, the combustion and processing of these fuels release significant amounts of carbon dioxide (CO_2), the primary anthropogenic greenhouse gas.[1] Every year, over 40 billion tons of CO_2 are emitted into the atmosphere from activities including power generation, cement production, and iron and steel manufacturing.[2–4] These emissions are directly associated with climate change phenomena, such as global warming, ocean acidification, and environmental issues, including urban smog and acid rain. To mitigate atmospheric CO_2 emissions, the 27 countries of the European Union have adopted binding reduction targets to address climate change in the coming decades.[5] In response to this challenge, several strategies based on solvents, sorbents, and membranes have emerged as key approaches to reduce CO_2 emissions. Among these methods, adsorption on solid sorbents, commonly referred to as carbon capture and storage (CCS),[6] has attracted increasing attention as a promising alternative to conventional amine-based solvent systems.[7] This versatile approach allows for CO_2 capture across a wide range of concentrations. The CO_2 concentration varies significantly depending on the gas mixture. Direct air capture (DAC) enables the extraction of CO_2 directly from ambient air, where its concentration is low, around 430 ppm (0.043%).[8] In contrast, large-scale industrial and energy sectors, including petroleum, coal, and natural gas, emit CO_2-rich streams with concentrations up to 50% in the gaseous mixture. For the latter, high-concentration capture

Université Claude Bernard Lyon 1, IRCELYON, UMR CNRS 5256, 2 avenue A. Einstein, 69626 Villeurbanne CEDEX, France.
E-mail: mickaele.bonneau@ircelyon.univ-lyon1.fr

methods include pre-combustion capture and oxy-fuel combustion capture with CO_2 concentration between 15–50% (150 000–500 000 ppm).[6] Post-combustion capture, on the other hand, deals with lower CO_2 concentrations, usually between 2 and 15%.[9,10] Numerous studies have investigated CO_2 adsorption in DAC and pre-combustion processes. However, fewer have focused on post-combustion adsorption, particularly at CO_2 concentrations below 5%, for which only limited literature is available. Low-CO_2 flue gas, typically containing 1–5% CO_2, originated from natural-gas-fired or high-air-flow combustion systems, and is significantly more challenging and energy-intensive to treat than higher-concentration industrial exhaust.[11]

Over the past decade, extensive research efforts have focused on testing and optimizing various porous materials for CO_2 capture,[1,12–14] including active carbons (ACs),[15,16] zeolites,[17,18] porous–organic polymers (POPs),[19,20] and metal–organic frameworks (MOFs).[21,22] From these studies, several criteria have emerged as essential prerequisites for efficient CO_2 adsorbents: (i) high CO_2 adsorption capacity, (ii) low regeneration temperature, (iii) high selectivity towards CO_2, (iv) chemical and thermal stability, and (v) scalability and cost-effectiveness.[23] Each class of material exhibits distinct advantages, yet none fully satisfies all these requirements simultaneously.[24] Siegelman *et al.* provided a qualitative assessment of the key performance metrics for these materials.[25] AC offer high stability and low cost but exhibit limited CO_2 selectivity and tunability. In contrast, POPs are highly tunable but challenging to regenerate and not yet commercially available. Zeolites combine high stability and large-scale production, but present only limited structural tunability. Furthermore, their hydrophilic nature leads to moderate selectivity towards CO_2. MOFs distinguish themselves by exhibiting both high selectivity for CO_2 and low regeneration temperatures. These materials, composed of organic linkers and metal nodes, offer exceptional tunability. Extensive research efforts have focused on reducing the synthesis costs and enabling large-scale production. Emphasis has been placed on employing non-toxic metals such as aluminium and zinc, and benign ligands like carboxylates and oxalates, alongside the use of water as a solvent. Eliminating filtration and washing steps further reduces energy consumption and waste generation by preventing the formation of undesired by-products.[26–28] Several MOFs are now synthesized at scale, including copper trimesate HKUST-1,[29] zirconium terephthalate UiO-66,[30] and zinc oxalate triazolate CALF-20.[31] Recently, our laboratory developed a single-step spray-drying synthesis of aluminium fumarate (Al-Fum), which removes the need for filtration and washing.[32] This method has also been extended to other aluminium-based MOFs such as MIL-120 and MIL-160.[33]

In this study, we evaluate the CO_2 adsorption capacity of porous materials under realistic flue gas conditions. Only scalable and non-toxic materials are tested through static and dynamic adsorption experiments. The initial step employs a volumetric apparatus to select materials with low affinity for water, a critical factor often overlooked in previous studies. The subsequent dynamic adsorption tests, conducted both in the absence and presence of water co-adsorption, enable identification of a material suitable for post-combustion capture at a low CO_2 concentration of 2.5%, a condition rarely investigated. Successive adsorption–desorption cycles confirm the robustness of the selected materials. This work provides valuable insights for developing selective, robust, and scalable CO_2 adsorbents capable of efficient operation under realistic post-combustion conditions.

Experimental

Materials

NaX, NaY, and NaMOR zeolites are obtained from Saint-Gobain. CALF-20 is provided by SINTEF. Al-Fum is synthesized by spray-drying according to the previously reported method,[32] and MIL-120 as well as MIL-160 are synthesized similarly using the spray-drying technique.[33] Deionized water is used in all static and dynamic adsorption experiments. For static CO_2 sorption experiments, pure CO_2 (>99.95%, Messer) is used. For dynamic adsorption experiments, a gas mixture of 5% CO_2 in N_2 (>4.97%, Air Liquide) is used.

Characterization of the adsorbents

X-ray diffraction (XRD) patterns are recorded using a Bruker (Siemens) D5000 diffractometer. Diffractograms are collected over a 2θ range of 5° to 50°, with a step size of 0.02° and a counting time of 1 second per step, employing CuKα radiation (λ = 1.54059 Å). N_2 physisorption measurements are performed on a Microtrac Belsorp Mini X instrument at 77 K. Prior to measurements, approximately 50 mg of each sample is outgassed overnight at 140 °C (Al-Fum, CALF-20, MIL-120, MIL-160) or 300 °C (NaMOR, NaX, NaY). Adsorption experiments are conducted within a relative pressure (P/P_0) range from 0 to 1. Equilibrium is defined by a pressure variation of less than 0.3% over 300 seconds at each data point. Characterization of the adsorbents is presented in the SI (Fig. S1 and Table S1).

Static sorption experiments

Volumetric static adsorption/desorption experiments of water and CO_2 are performed using a commercially available Microtrac Belsorp Max II. Before the experiment, materials are activated under vacuum at 140 °C or 300 °C, depending on the material, using a BelPrep Vac. Isotherms are then obtained by applying incremental pressures of water or CO_2 within the cell. Thermodynamic equilibrium is considered achieved when the total pressure variation within the cell falls below 0.3% over 300 seconds. Isotherms are performed at different temperatures (0, 10, and 20 °C) to apply Polanyi's adsorption potential theory and to validate the establishment of thermodynamic equilibrium (SI).[34]

Dynamic sorption experiments

Dynamic breakthrough adsorption experiments are conducted using a custom-built apparatus described in the SI

(Scheme S1), and consists of an adaptation of the setup described elsewhere.[35] The column consists of a glass tube with an internal diameter of 4 mm, packed with approximately 250 mg of nanoporous material to a height of 4 cm, depending on the powder density. Before the adsorption, the materials are activated under N_2 flow at 140 °C (the maximum temperature allowed by the setup) to remove any adsorbed molecules. The CO_2 concentration in the inlet stream (C_0) is verified before each breakthrough experiment by bypassing the column and measuring with a CO_2 detector (Vaisala Carbocap with CO_2 probe GMP251). Adsorption experiments are performed at atmospheric pressure (≈100 kPa) and at a constant temperature of 20 °C. For dry adsorption experiments, a mixture containing 2.5% CO_2 (100 mL min^{-1} total flow) is generated by mixing a 50 mL min^{-1} flow of 5% CO_2 in N_2 with 50 mL min^{-1} pure N_2 (resulting contact time τ = 0.3 s). CO_2 concentrations in the outlet flow (C) are continuously monitored by the detector. For wet adsorption experiments, the pure N_2 dilution flow is replaced with a 50 mL min^{-1} N_2 flow at 99% relative humidity (RH) generated using a Flexi Wet 200 apparatus (Setaram), yielding an overall flow of 100 mL min^{-1} with 2.5% CO_2 and 50% RH (p_{H_2O} = 1.15 kPa). Water vapor concentration is measured by a calibrated hygrometer. Following adsorption, regeneration is carried out by flowing a pure N_2 flow of 100 mL min^{-1} while heating the column to the target temperature with a controlled ramp rate. Multiple adsorption/regeneration cycles are performed either under dry or humid conditions to assess material stability. To compare the different water adsorption capacities, every breakthrough graph is presented for 1 gram of dried adsorbent (min g^{-1}). A symbol "≈" is added before the numeric value, which points to the error evaluated at 5%. The MOF/zeolite particles (300–600 μm) are sufficiently small to minimize intraparticle diffusion resistance, and external mass transfer is adequate at the low total flow rate of 100 mL min^{-1} through a 4 mm diameter column. Under our conditions, the superficial velocity is low (~0.083 m s^{-1}), resulting in a Sherwood number indicating efficient gas–solid mass transfer. The bed height (4–8 cm) promotes near plug-flow behavior, and the modest pressure drop (1.05 bar) confirms the absence of flow constraints. Heat generated during adsorption is minimal due to the low CO_2 loading and moderate adsorption enthalpy of MOF/zeolite materials, yielding an estimated temperature rise of <0.5 K. Therefore, under these conditions, breakthrough behavior is governed by adsorption equilibrium, with no significant mass- or thermal-transfer limitations.

Results and discussion

Static adsorption experiments

Static CO_2 adsorption isotherms are performed at three different temperatures using three sodium-exchanged zeolites and four scalable MOFs. To verify thermodynamic equilibrium, Polanyi's adsorption potential theory is applied. Polanyi's adsorption potential theory describes adsorption as the filling of a potential field near a solid surface, rather than as the simple layer-by-layer attachment of molecules.[36] In microporous materials in particular, adsorption is therefore interpreted as the volume filling of pores. For a given adsorbent–adsorbate system, when the amount adsorbed is plotted as a function of the adsorption potential, isotherms measured at different temperatures collapse onto a single curve, commonly referred to as the master curve. The characteristic curves are obtained for almost all adsorbate/adsorbent pairs, confirming the reach of thermodynamic equilibrium (Fig. S2). Only MIL-120 differs from other materials and a deviation is observed. Thermodynamic equilibrium is not reached for this material, highlighting diffusional constraints during CO_2 adsorption. From the isotherms performed at 20 °C, no plateau is observed for any of the materials (Fig. 1a). This suggests that the adsorption is not complete, as the saturated vapor pressure of CO_2 at 20 °C (Pv_{sat} = 3485.1 kPa) is not reached at the maximum operating pressure of 100 kPa. The highest adsorption capacities are recorded for NaY and NaX, with 6.14 and 5.85 mmol g^{-1}, respectively, followed by CALF-20 (3.88 mmol g^{-1}) and MIL-160 (3.64 mmol g^{-1}). NaMOR adsorbs 3.24 mmol g^{-1}. The lowest capacities are observed for Al-Fum and MIL-120, with adsorption capacities of 2.60 and 1.84 mmol g^{-1}, respectively. Using the CO_2 concentration in the application case of low flue gas conditions (2.5%), the adsorption order changes: NaX maintains a high capacity of 3.15 mmol g^{-1} (54% maintained), whereas the capacity of NaY

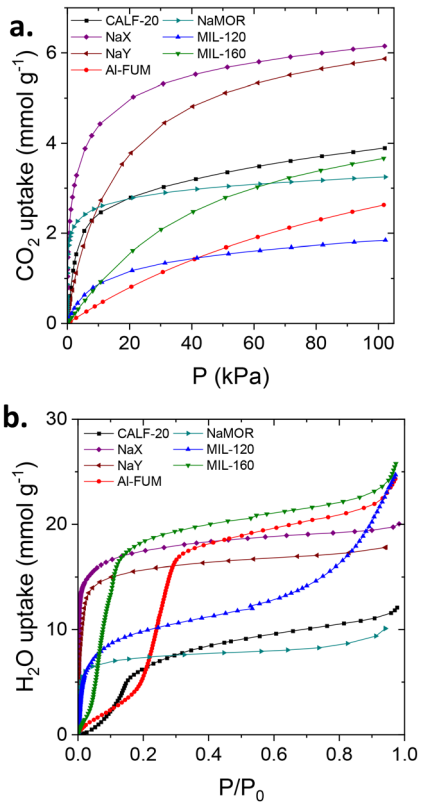

Fig. 1 CO_2 (a) and H_2O (b) adsorption isotherms at 20 °C.

decreases noticeably to 1.02 mmol g^{-1} (17% maintained), nearly six times lower than at pure CO_2 concentration. NaMOR and CALF-20 show the second and third highest adsorption capacities, with 2.19 and 1.44 mmol g^{-1}, respectively. MIL-120 adsorbs 0.37 mmol g^{-1}. Finally, the lowest capacities under these conditions are observed for MIL-160 and Al-Fum, adsorbing 0.23 and 0.11 mmol g^{-1}, respectively.

The study of water adsorption is essential to mimic realistic flue gas conditions, which typically contain water vapor around a relative humidity of 50%. The objective is to identify a nanoporous sorbent that minimizes water adsorption, allowing maximized CO_2 uptake, and can be easily regenerated at low temperature. Materials exhibiting Type I isotherms characterize strong water affinity, resulting in temperature and energy-demanding regeneration. Conversely, materials displaying Type V isotherms tend to interact less with water molecules, facilitating regeneration under mild conditions (typically 80 °C).

Water adsorption experiments are performed at 20 °C for all materials (Fig. 1b). Type-I isotherms are obtained for the three zeolites, whereas the four MOFs exhibit Type-V isotherms. To access the strength of interaction between water molecules and the adsorbent, and thereby predict the regeneration behavior, Henry's constants (K_H) are derived from the low-pressure region of each isotherm (Fig. 2). As expected, based on the isotherm type, the three zeolites display high K_H values, indicative of strong adsorbate–adsorbent interactions. The highest K_H value is obtained for NaY (673.2 mmol g^{-1} kPa^{-1}). In contrast, the MOFs show significantly lower K_H values (<40 mmol g^{-1} kPa^{-1}), with CALF-20 exhibiting the weakest affinity (4.6 mmol g^{-1} kPa^{-1}). The α parameter (defined as the relative pressure P/P_0 at which half of the total water uptake is reached[37]) supports the same trend, confirming the pronounced hydrophilicity of the zeolites and the moderate hydrophilicity of the MOFs.

For a relative humidity of 50%, MIL-160 adsorbs approximately 20.5 mmol g^{-1} of water while Al-Fum and NaX adsorb 18.9 and 18.6 mmol g^{-1}, respectively. Conversely, CALF-20 and NaMOR exhibit the lowest water adsorption capacities, with values of 9.0 and 7.8 mmol g^{-1}, respectively.

Although zeolites, particularly NaX and NaMOR, exhibit high CO_2 adsorption capacities, their strong hydrophilicity limits their applicability for low CO_2 concentrations. In addition, the regeneration temperature required to fully desorb water molecules is significantly higher than that of MOFs, reaching up to 300 °C.[38,39]

Dynamic adsorption experiments

Dynamic adsorption experiments are conducted to evaluate the effect of N_2 in flue gas on CO_2 adsorption, and to assess the selectivity between water and CO_2. Zeolites exhibiting strong hydrophilicity and high regeneration temperatures as evaluated using static adsorption experiments, only MOFs are selected for breakthrough adsorption experiments.

To confirm the adsorption capacities obtained from static experiments and the selectivity towards N_2, dynamic adsorption experiments with a CO_2 concentration of 2.5% under dry conditions (Fig. 3) are first performed. All materials show characteristic symmetric S-shaped breakthrough profiles, indicative of plug-flow-like behavior. Integration of breakthrough curves shows that Al-Fum, the least effective MOF in this series, exhibits CO_2 breakthrough after approximately one minute per gram and adsorbs only ≈0.10 mmol g^{-1} of CO_2. This value is consistent with static isotherm data, and confirms negligible N_2 adsorption and unperturbed CO_2 capture. Similarly, MIL-160 and MIL-120 show excellent agreement between dynamic and static adsorption, with capacities of ≈0.27 and ≈0.39 mmol g^{-1}, *versus* 0.23 and 0.37 mmol g^{-1}, respectively, from static adsorption experiments. Notably, CALF-20 completely adsorbs CO_2 without any effluent detection for more than 10 minutes per gram. CALF-20 demonstrates the highest CO_2 capacity with ≈1.43 mmol g^{-1}, in close agreement with its isotherm value of 1.44 mmol g^{-1}. These results highlight the selective CO_2 adsorption of CALF-20 with

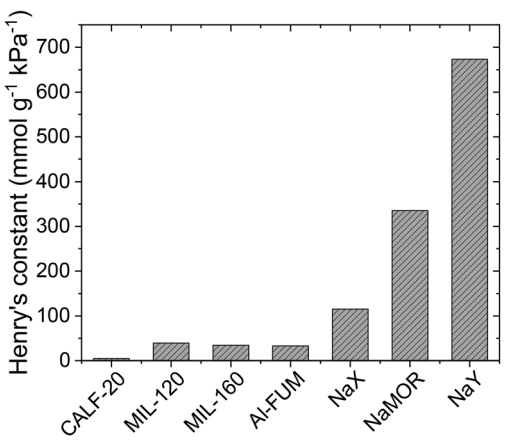

Fig. 2 Henry's constant obtained from H_2O isotherms performed at 20 °C.

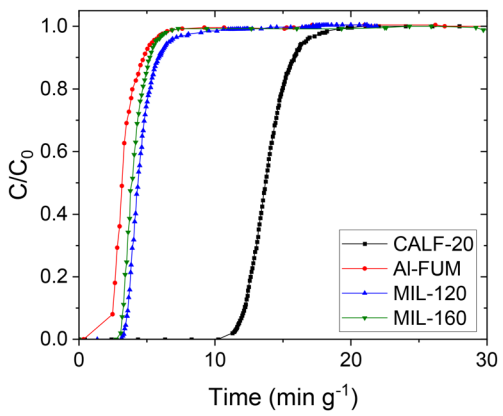

Fig. 3 Breakthrough adsorption experiments with a dry 2.5% CO_2 concentration flow at 20 °C.

no competition from N_2 and confirm its superior performance, achieving almost four times the capacity of MIL-120, the second-best material.

In order to evaluate the regeneration performance of these materials, and thus the working capacity of the different MOFs, three adsorption cycles at 20 °C followed by regeneration at 80 °C under N_2 are carried out. As expected, CALF-20 exhibits full desorption of previously adsorbed CO_2, allowing complete regeneration. The second and third cycles show consistent adsorption capacities of ≈1.61 mmol g^{-1} and ≈1.50 mmol g^{-1}, respectively (Fig. 4). MIL-160 and MIL-120 display similar behavior, achieving full CO_2 regeneration, with a lower cycled working capacity (Fig. S3a and b). Breakthrough experiment performed on MIL-120 confirms the diffusional constraint of CO_2 within the porous system, as already observed using static adsorption experiments. Indeed, during the regeneration step, while the outlet flow reaches 0 mmol g^{-1} of CO_2 after 11 minutes per gram under N_2, more than 30 min per gram are necessary to fully desorb CO_2 (Fig. S4).

The adsorption of CO_2 under model flue gas conditions requires evaluating the competitive adsorption behavior of CO_2 and H_2O. Breakthrough experiments (inlet flow of 2.5% CO_2 and 50% RH) are conducted using CALF-20, the material with the highest CO_2 adsorption capacity. Adsorption of CO_2 and H_2O occurs in three steps (Fig. 5, zoom in Fig. S5). During the first stage, both CO_2 and H_2O are co-adsorbed during the initial 10 minutes per gram, resulting in the uptake of ≈1.49 mmol g^{-1} of CO_2. This value agrees closely with that obtained under dry conditions (≈1.43 mmol g^{-1}) and with the adsorption isotherm, thereby confirming the robustness of CALF-20 for CO_2 capture under realistic flue gas conditions. In the second stage, a CO_2 roll-up is observed, leading to the complete desorption of CO_2 (≈1.45 mmol g^{-1}) even as water continues to adsorb. Water begins to break after approximately one hour per gram, with its outlet concentration gradually increasing before a sharp rise after 3.5 hours per gram. In the third and final stage, equilibrium is reached after 4 hours per gram, at which point the outlet composition matches that of the inlet gas for both CO_2 and H_2O. Integration of the breakthrough curve for H_2O yields a total uptake of ≈8.70 mmol g^{-1}, which is in good agreement with static adsorption measurements on CALF-20 at 50% RH (9.0 mmol g^{-1}). Regeneration of the material is achieved by switching the gas feed to pure N_2 while increasing the temperature gradually to 80 °C (5 °C min^{-1}). During this heating step, no CO_2 could be detected in the outlet flow as it is already fully desorbed during the later step, while ≈8.90 mmol g^{-1} of water is desorbed. This value is consistent with the amount adsorbed during the uptake step, confirming the complete regeneration of CALF-20.

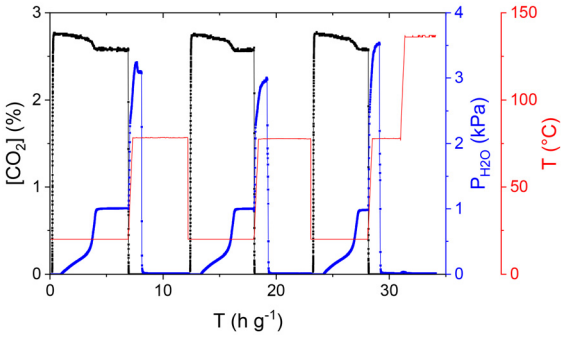

Fig. 5 Cycles of adsorption/regeneration with a 2.5% CO_2 concentration flow and relative humidity of 50% on CALF-20 at 20 °C.

To confirm the total regeneration of CALF-20 at 80 °C, three consecutive adsorption cycles under realistic flue gas conditions followed by regeneration at 80 °C are performed (Fig. 5). The breakthrough profiles for both CO_2 and H_2O are consistent across cycles, with similar adsorption capacities observed. These results demonstrate the full regeneration and excellent working capacities at equilibrium of CALF-20 after multiple adsorption/regeneration cycles for CO_2 capture under low concentration CO_2 conditions.

Compared with Al-Fumarate and MIL-series MOFs, which often present open metal sites or polar functional groups that strongly interact with water, CALF-20's pore environment is dominated by hydrophobic triazolate linkers and no open metal sites, reducing initial water binding and maintaining CO_2 uptake under moderate humidity.[40] Binary adsorption studies highlight that CALF-20's CO_2 adsorption is retained over a broader humidity range, whereas water uptake in other materials is less affected by CO_2.[41] The mechanism behind CALF's 20 performances was already discussed by Ho and Paesani.[42] CO_2 binding is thermodynamically more favorable under dilute conditions and humidity, and the relatively hydrophobic nature of the framework suppresses H_2O uptake at low to moderate humidity. The presence of CO_2 slows H_2O reorientation dynamics and lowers water entropy, indicating reduced H_2O mobility, while H_2O enhances CO_2 reorientation and can increase its adsorption. These competitive yet interdependent thermodynamic and dynamic effects likely underpin the experimentally observed CO_2 "roll-up" behavior under humid conditions.

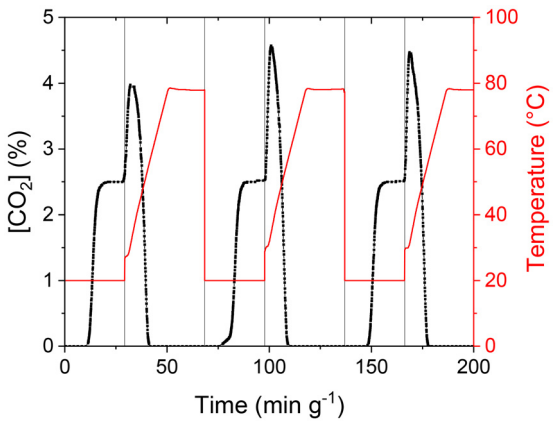

Fig. 4 Cycles of adsorption/regeneration with a dry 2.5% CO_2 concentration flow on CALF-20 at 20 °C.

Conclusions

In this study, various scalable and environmentally friendly microporous materials are evaluated for CO_2 capture under realistic post-combustion flue gas conditions. Static adsorption results showed that zeolites exhibit high CO_2 adsorption capacities and low total water uptake. However, their pronounced hydrophilicity, confirmed by pure Type-I isotherms and high Henry's constant, indicates a strong affinity for water. This affinity inevitably leads to competitive adsorption between water and CO_2 under realistic conditions. Conversely, although MOFs such as MIL-160, MIL-120, and Al-Fum adsorb moderate amounts of CO_2 alongside significant water uptake, their Type-V water adsorption isotherms and significantly lower Henry's constants relative to zeolites suggest a reduced affinity for water. Among these materials, CALF-20 stands out by demonstrating low water adsorption coupled with high CO_2 uptake. This performance is validated in dynamic adsorption experiments using CO_2 under post-combustion conditions with a concentration of 2.5%, aligning well with the results of static experiments for equivalent concentrations. No competitive adsorption between N_2 and CO_2 is observed, confirming the excellent selectivity of CALF-20 towards CO_2. Moreover, successive adsorption–regeneration cycles demonstrated the good stability of the material in dry conditions. Dynamic adsorption experiments under realistic flue gas conditions demonstrate that CALF-20 maintains its high CO_2 adsorption capacity and cycle reproducibility even in the presence of water vapor. Despite these positive results, long-term stability over several years must be established to confirm its suitability for practical applications.

This study represents an effective pathway for CO_2 capture under realistic conditions. Future work should focus on porous materials with reduced water affinity and enhanced CO_2 capacity to advance this technology. Such developments are expected to contribute significantly to reducing atmospheric CO_2 emissions and addressing climate change mitigation targets in the coming years.

Author contributions

The manuscript was written through contributions of all authors. All authors have given approval to the final version of the manuscript. T. A.: data curation, formal analysis, investigation, visualization, writing – original draft, writing – review & editing. M. B.: formal analysis, investigation, writing – review & editing. C. C.: data curation, formal analysis. C. D.: data curation, methodology. D. F.: funding acquisition, supervising, writing – review & editing.

Conflicts of interest

The authors declare that they have no known competing financial interests or personal relationships that could have appeared to influence the work reported in this paper.

Data availability

All data from this study are available within the article and its supplementary information (SI). Supplementary information: additional experimental data, including physisorption isotherms, characterization data, and breakthrough experiment details. See DOI: https://doi.org/10.1039/d6dt00282j.

All single gas isotherms are also available in AIF format. Any further data are available from the corresponding author upon request.

Acknowledgements

This research was funded by CET Partnership, the Clean Energy Transition under the 2023 joint call for research proposals, co-funded by the European Commission (GA No. 101069750), and with the funding organizations https://cet-partnership.eu/funding-agencies-and-call-modules.

References

1 S. Foorginezhad, F. Weiland, Y. Chen, S. Hussain and X. Ji, *Renewable Sustainable Energy Rev.*, 2025, **215**, 115589.
2 E. J. L. Chappin and G. P. J. Dijkema, *Technol. Forecast. Soc. Change*, 2009, **76**, 358–370.
3 E. Benhelal, E. Shamsaei and M. I. Rashid, *J. Environ. Sci.*, 2021, **104**, 84–101.
4 C. Xu and D. Cang, *J. Iron Steel Res. Int.*, 2010, **17**, 1–7.
5 Directive (EU) 2023/1791 of the European Parliament and of the Council of 13 September 2023 on Energy Efficiency and Amending Regulation (EU) 2023/955 (Recast).
6 D. Bose, R. Bhattacharya, T. Kaur, R. Pandya, A. Sarkar, A. Ray, S. Mondal, A. Mondal, P. Ghosh and R. I. Chemudupati, *Carbon Capture Sci. Technol.*, 2024, **12**, 100238.
7 S. A. Mazari, B. S. Ali, B. M. Jan, I. M. Saeed and S. Nizamuddin, *Int. J. Greenhouse Gas Control*, 2015, **34**, 129–140.
8 S. Mahajan and M. Lahtinen, *J. Environ. Chem. Eng.*, 2022, **10**, 108930.
9 E. Favre, *J. Membr. Sci.*, 2007, **294**, 50–59.
10 A. Rana and J. M. Andino, *Catalysts*, 2025, **15**, 273.
11 R. W. Baker, B. Freeman, J. Kniep, X. Wei and T. Merkel, *Int. J. Greenhouse Gas Control*, 2017, **66**, 35–47.
12 G. Singh, J. Lee, A. Karakoti, R. Bahadur, J. Yi, D. Zhao, K. AlBahily and A. Vinu, *Chem. Soc. Rev.*, 2020, **49**, 4360–4404.
13 J. M. Huck, L.-C. Lin, A. H. Berger, M. N. Shahrak, R. L. Martin, A. S. Bhown, M. Haranczyk, K. Reuter and B. Smit, *Energy Environ. Sci.*, 2014, **7**, 4132–4146.
14 H. Zentou, B. Hoque, M. A. Abdalla, A. F. Saber, O. Y. Abdelaziz, M. Aliyu, A. M. Alkhedhair, A. J. Alabduly and M. M. Abdelnaby, *Carbon Capture Sci. Technol.*, 2025, **15**, 100386.

15 P. Arjona-Jaime, R. Morales-Ospino, M. T. Izquierdo, L. F. Chazaro-Ruiz, A. Celzard, R. Rangel-Mendez and V. Fierro, *Chem. Eng. J.*, 2025, **525**, 170349.
16 J. Serafin and B. Dziejarski, *Environ. Sci. Pollut. Res.*, 2024, **31**, 40008–40062.
17 K. B. Jivrakh, A. M. Varghese, S. Ehrling, S. Kuppireddy, K. Polychronopoulou, R. K. Abu Al-Rub, N. Alamoodi and G. N. Karanikolos, *Chem. Eng. J.*, 2024, **497**, 154674.
18 W. Rahmah, G. T. M. Kadja, M. H. Mahyuddin, A. G. Saputro, H. K. Dipojono and I. G. Wenten, *J. Environ. Chem. Eng.*, 2022, **10**, 108707.
19 K. S. Song, P. W. Fritz and A. Coskun, *Chem. Soc. Rev.*, 2022, **51**, 9831–9852.
20 Z. Zhong, X. Wang and B. Tan, *Chem. – Eur. J.*, 2025, **31**, e202404089.
21 K. Fan, Y. Wang, C. Tian, X. Guan, X. Luo and Y. Zhou, *Chem. Eng. J.*, 2025, **522**, 167344.
22 H. Mahdavi, A. Robin, N. T. Eden, A. Khosravanian, M. M. Sadiq, K. Konstas, S. J. D. Smith, X. Mulet and M. R. Hill, *Langmuir*, 2024, **40**, 17387–17395.
23 R. Singh, L. Wang, K. Ostrikov and J. Huang, *Adv. Mater. Interfaces*, 2024, **11**, 2202290.
24 M.-M. Jin, Y.-X. Li, C. Gu, X.-Q. Liu and L.-B. Sun, *AIChE J.*, 2020, **66**, e16645.
25 R. L. Siegelman, E. J. Kim and J. R. Long, *Nat. Mater.*, 2021, **20**, 1060–1072.
26 D. Chakraborty, A. Yurdusen, G. Mouchaham, F. Nouar and C. Serre, *Adv. Funct. Mater.*, 2024, **34**, 2309089.
27 Z. Han, Y. Yang, J. Rushlow, J. Huo, Z. Liu, Y.-C. Hsu, R. Yin, M. Wang, R. Liang, K.-Y. Wang and H.-C. Zhou, *Chem. Soc. Rev.*, 2025, **54**, 367–395.
28 K. Pobłocki, J. Drzeżdżon, B. Gawdzik and D. Jacewicz, *Green Chem.*, 2022, **24**, 9402–9427.
29 C. McKinstry, E. J. Cussen, A. J. Fletcher, S. V. Patwardhan and J. Sefcik, *Chem. Eng. J.*, 2017, **326**, 570–577.
30 Y. Zhao, Q. Zhang, Y. Li, R. Zhang and G. Lu, *ACS Appl. Mater. Interfaces*, 2017, **9**, 15079–15085.
31 J.-B. Lin, T. T. T. Nguyen, R. Vaidhyanathan, J. Burner, J. M. Taylor, H. Durekova, F. Akhtar, R. K. Mah, O. Ghaffari-Nik, S. Marx, N. Fylstra, S. S. Iremonger, K. W. Dawson, P. Sarkar, P. Hovington, A. Rajendran, T. K. Woo and G. K. H. Shimizu, *Science*, 2021, **374**, 1464–1469.
32 M. Perbet, T. Aumond, C. Collomb, C. Daniel, I. Imaz, G. Pena, D. Maspoch, T. Michon, R. Morales-Ospino, V. Fierro, E. A. Quadrelli and D. Farrusseng, *Ind. Eng. Chem. Res.*, 2025, **64**, 6541–6549.
33 M. Perbet, T. Michon, E. A. Quadrelli, M. Bonneau and D. Farrusseng, *Chem. Commun.*, 2025, **61**, 12562–12565.
34 T. Aumond, R. Manokaran, J. Eck, O. Ergincan, C. Daniel, D. Farrusseng and B. Coasne, *Ind. Eng. Chem. Res.*, 2024, **63**, 19375–19397.
35 T. Aumond, C. Daniel, C. Collomb, K. Dedecker, M. Drobek, A. Julbe and D. Farrusseng, *New J. Chem.*, 2025, **49**, 5390–5401.
36 C. Daniel, T. Aumond, C. Collomb, B. Coasne and D. Farrusseng, *ChemRxiv*, 2026, preprint, DOI: 10.26434/chemrxiv.15000631/v1.
37 J. Canivet, J. Bonnefoy, C. Daniel, A. Legrand, B. Coasne and D. Farrusseng, *New J. Chem.*, 2014, **38**, 3102–3111.
38 L. Presa, J. L. Costafreda, D. A. Martín and I. Díaz, *Molecules*, 2020, **25**, 1220.
39 Ş. Ç. Sayılgan, M. Mobedi and S. Ülkü, *Microporous Mesoporous Mater.*, 2016, **224**, 9–16.
40 R. Oktavian, R. Goeminne, L. T. Glasby, P. Song, R. Huynh, O. T. Qazvini, O. Ghaffari-Nik, N. Masoumifard, J. L. Cordiner, P. Hovington, V. Van Speybroeck and P. Z. Moghadam, *Nat. Commun.*, 2024, **15**, 3898.
41 N. Constant, G. Liske, S. S. Ravuru, A. Puliyanda, V. Pugnet, A. O. Sanchez, S. R. Chavan, P. Llewellyn, J. A. Sawada and A. Rajendran, *Ind. Eng. Chem. Res.*, 2025, **64**(3), 1712–1729.
42 C.-H. Ho and F. Paesani, *ACS Appl. Mater. Interfaces*, 2023, **15**, 48287–48295.